communications engineering

Article

A Nature Portfolio journal

Article in Press

https://doi.org/10.1038/s44172-026-00787-1

Inverse design of metamaterials for wideband multi-beam former

Check for updates

Ilir Gashi [1] ✉, Scott Twiddy[2,3], Zachary Nelson [2,3], Stefano Maci[1] & Matteo Albani[1]

The demand for compact beam-steering solutions has driven interest in gradient-index (GRIN) lenses, which shape wavefronts via spatially varying dielectric properties. Additive manufacturing enables their fabrication, but a central challenge remains: solving the inverse problem of determining the volumetric permittivity distribution for a desired field transformation. Unlike voxel-by-voxel topology optimization requiring thousands of full-wave simulations, our approach targets smooth GRIN profiles for propagation-based devices, reducing optimization to minutes on a standard computer. Here, we present an inverse-design framework that optimizes the geometrical optics propagation equations directly. We experimentally demonstrate the method by realizing a multi-feed GRIN lens based on a three-dimensional gyroid architecture fabricated via additive manufacturing. The device enables continuous beam scanning over a ±35° range with 33% fractional bandwidth, low scan loss, and excellent beam fidelity. Our results establish a direct pathway from electromagnetic functionality to manufacturable metamaterial devices, enabling scalable wavefront engineering

The ability to manipulate electromagnetic wavefronts is the basis of modern communication, radar, and imaging systems. Traditional optical components and electronic beamforming networks are inherently constrained by fundamental trade-offs between performance, bandwidth, complexity, and cost. Graded-index (GRIN) optics, which guide waves through a spatially tailored refractive index, offer a transformative alternative by enabling flat form factors, intrinsic broadband operation, and direct impedance matching[1–4], and their analysis is typically performed by a Geometrical Optics (GO) ray tracing algorithm[5]. Although the concept of GRIN optics is well-established, its practical implementation has been revolutionized by recent advances in planar optics and metasurfaces[6–10]. Furthermore, breakthrough additive manufacturing techniques–such as vision-controlled material jetting[11,12] and functional 3D printing of complex meta-structures[13–15]–now permit the fabrication of intricate three-dimensional dielectric structures with unprecedented precision. This technological progress, however, shifts the central challenge to the computational domain: solving the inverse problem of determining the volumetric permittivity distribution that transforms a prescribed input field into a desired output field. Unlike voxel–by–voxel topology optimization[16,17] requiring thousands of full–wave simulations and tens of hours of HPC computation, our approach addresses a different regime: continuous, smoothly varying GRIN profiles for propagation–based microwave devices. We parametrize the design with only nine control points and solve the Eikonal equation directly via the Lax–Friedrichs sweeping method, reducing the optimization to minutes on a standard desktop computer. This parametric GO–based approach is therefore complementary to, rather than competitive with, high–resolution adjoint methods for scattering structures.

This inverse design problem is inherently high-dimensional and nonlinear. Traditional approaches relying on direct ray-tracing become computationally prohibitive for volumetric designs, particularly when modeling complex wave phenomena such as caustics or multipath propagation. Recent literature has extensively explored inverse design in nano-photonics and meta-optics[18–20], employing diverse strategies ranging from topology optimization[21] and adjoint methods[22] to deep-learning-enabled self-design[23]. While these advancements demonstrate the power of complete phase and amplitude control in 2D and 3D integrated optics[24–27], they often lack the generality and efficiency required for the rapid optimization of large-scale, multi-functional microwave devices.

The specific case treated in this work is based on the realization of the kernel of a one-dimensional spatial Fourier transform. We design a flat, planar optical box where one boundary is populated by discrete input ports supporting localized modal excitations, while the opposite boundary enforces a continuous linear phase distribution. This formulation provides a clear physical link between discrete port excitation and far-field beam steering through a continuous Fourier-like transformation, similar to concepts used in on-chip GRIN meta-lenses and spaceplate-compressed systems[28,29]. To address the computational bottleneck, we introduce a general inverse-design framework that operates directly on the underlying partial differential equations of geometrical optics wavefront propagation–namely, the Eikonal and transport equations. By formulating

[1]Department of Information Engineering and Mathematics, University of Siena, Siena, Italy. [2]Inkbit, Medford, MA, USA. [3]These authors contributed equally: Scott Twiddy, Zachary Nelson. ✉e-mail: ilir.gashi2@unisi.it

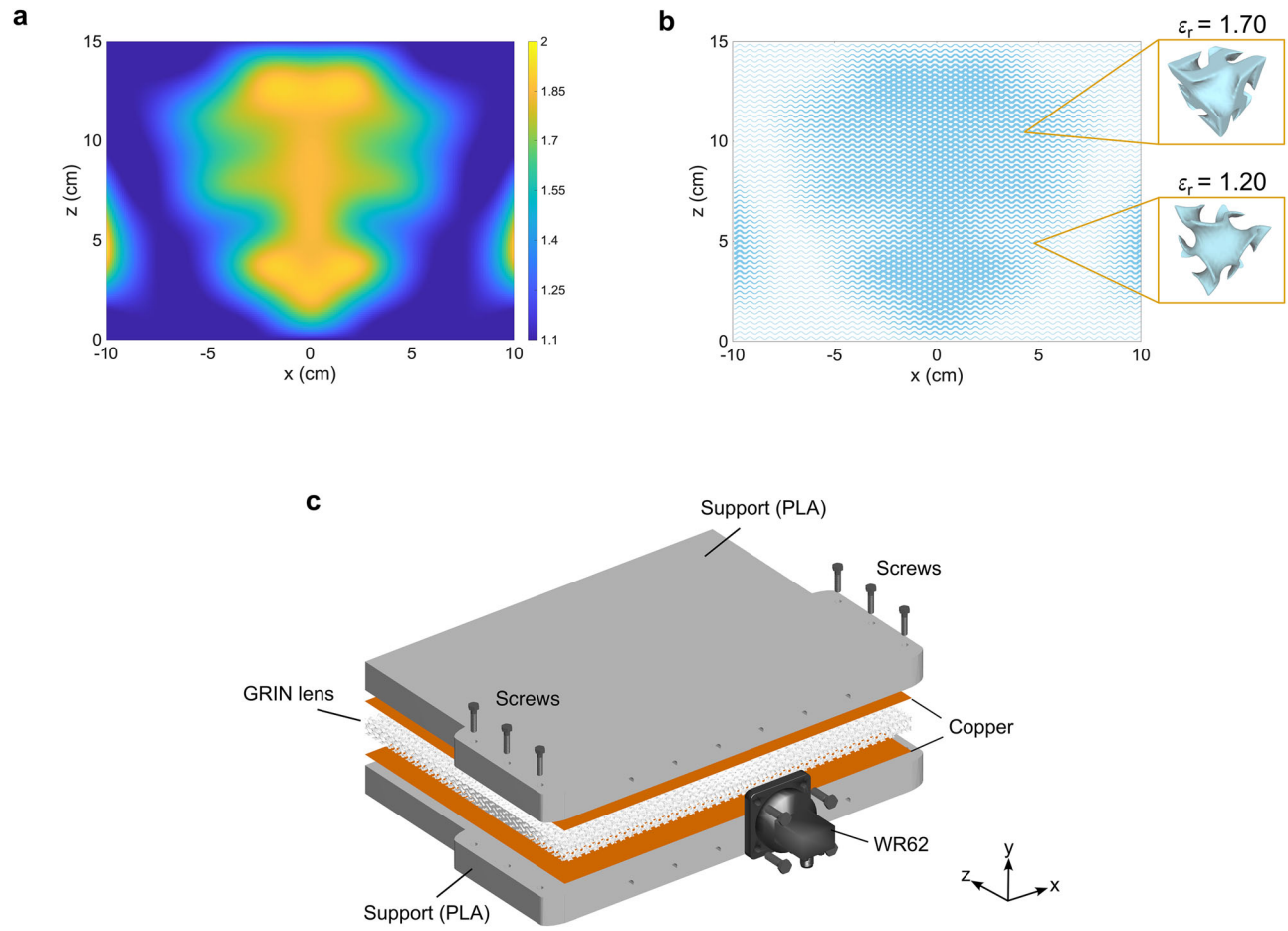


Fig. 1 | Design, realization, and experimental implementation of the GRIN lens. **a** Numerically designed spatial distribution of the graded refractive index (GRIN) obtained from the inverse-design framework. **b** Physical realization of the GRIN profile using a graded gyroid unit-cell architecture, enabling a continuous effective permittivity distribution. **c** Exploded view of the experimental parallel-plate waveguide setup, showing the GRIN lens integrated between copper plates and mechanically supported by PLA fixtures; waveguide (WR62) ports can be laterally translated to excite different input positions.

the design as a constrained optimization problem, our approach circumvents the limitations of traditional ray-tracing or predefined ray mappings[30,31]. Computational efficiency is achieved through the integration of the Lax-Friedrichs sweeping method[32], a fast numerical solver that enables rapid performance evaluation within the optimization loop.

We demonstrate the effectiveness of this framework by designing, fabricating, and experimentally validating a multi-port GRIN lens antenna operating across the Ku-band (13–18 GHz). The lens comprises a planar array of input ports; exciting a single port generates a directive fan beam in the far field, with the steering angle determined by the port location. The entire design is completed in minutes on a standard desktop computer and achieves beam scanning over ±35°. The computed permittivity distribution is physically realized using a mechanically robust, graded gyroid unit-cell architecture, leveraging modern inverse design of composite material properties for additive manufacturing[11].

This multi-feed GRIN lens presents a compelling alternative to conventional beamforming architectures, such as the Rotman lens[33] or the Butler matrix[34], offering a simpler, more compact, and wider-bandwidth solution for modern wireless communications[35]. Its ability to generate discrete, steerable fan beams with high crossover gain renders it directly applicable to multi-beam satellite communication terminals, automotive radar with segmented field-of-view, and fixed-beam switching for wireless access points. By establishing an efficient and direct pathway from system-level functionality to a validated, manufacturable device, this work bridges a critical gap in the development of next-generation beam-steering components.

Results

In this section, we present the complete experimental and numerical characterization of the inverse-designed GRIN lens. We first describe the computational design process and its translation into a physical metamaterial architecture. We then detail the fabrication of the lens using Vision-Controlled Jetting (VCJ) and its integration into a parallel-plate waveguide (PPW) measurement setup. The physical mechanism underlying the device operation is visualized through near-field simulations, which reveal how the graded-index profile transforms cylindrical wavefronts into tilted plane waves across the 13–18 GHz band. Finally, we validate the far-field radiation performance, demonstrating discrete beam steering over a ±35° range with low scan loss and excellent agreement between simulations and measurements.

From computational design to fabricated metamaterial

The path from the electromagnetic objective function to the physical device begins with the computational inverse design. Our framework, treating the permittivity distribution as the optimization variable, converged on a spatially varying GRIN map that encodes the multi-beam steering functionality. The resulting two-dimensional refractive index profile is revealed in Fig. 1a. It is not a simple lens analog, but a complex topological landscape where smooth gradients manipulate the wavefront. Distinctive features include regions of focused gradient curvature that gradually blend to a unity refractive index adjacent to each input port to avoid modal mismatch. This contoured GRIN profile, computationally derived in a few minutes on a standard personal computer, serves as the foundational blueprint, specifying

the exact local dielectric constant required at every voxel to transform a point-source emission from any input port into a perfectly collimated, angled fan beam.

Translating this abstract numerical design into a manufacturable structure required a metamaterial strategy. Direct fabrication of a material with continuously varying bulk permittivity remains impractical; instead, we employed a graded, three-dimensional gyroid-unit-cell architecture. The gyroid, a triply periodic minimal surface, offers a mechanically robust, self-supporting scaffold whose effective permittivity can be precisely tuned by varying its volumetric filling fraction. By mapping the target permittivity value at each point in the design (Fig. 1a) to a specific thickness of the gyroid wall, we generated a continuous digital model in which the intricate gyroid lattice smoothly transitions from sparse (low $\varepsilon_r \approx 1.1$) to dense (high $\varepsilon_r \approx 2.0$). We emphasize that the electromagnetic design and the resulting permittivity map (Fig. 1a) are strictly two–dimensional (in the *xz*-plane). The three–dimensional gyroid architecture (Fig. 1b) serves exclusively as a fabrication metamaterial - it locally synthesises the required 2D effective permittivity through spatially varying filling fractions, while the parallel–plate waveguide height ($< \lambda/2$) ensures no vertical field variation.

Fabrication via vision-controlled jetting

The practical realization of the intricate, spatially-varying permittivity profile requires a manufacturing technology capable of translating a digital gradient into a physical dielectric structure with high fidelity. To meet these demands, the multi-feed GRIN lens was fabricated using an advanced inkjet-based additive manufacturing process known as VCJ[11,12]. This process utilizes a closed-loop high-speed 3D vision system that captures a depth map of the deposited surface after each layer. The system automatically compensates for any deviations from the ideal geometry by locally adapting the amount of resin deposited in the subsequent layer, ensuring high dimensional accuracy and eliminating the need for mechanical planarization. This contactless approach enables the use of material chemistries that would otherwise be incompatible with traditional inkjet 3D printing.

For this work, the lens was manufactured using a low-loss dielectric polymer from Inkbit's Cyclic Olefin Thermoset (COT) material family, a polyolefin-based thermoset specifically formulated for high-frequency applications. By mapping the target permittivity value at each point in the design to a specific volumetric filling fraction of the gyroid lattice, the effective permittivity of the constituent COT material is precisely tuned across the desired range ($\varepsilon_r \approx 1.1$ to 2.0), creating a smooth and continuous gradient. The digital model of this graded lattice was voxelized and sliced, then manufactured with a minimum positive feature size of approximately 300 μm and fabricated within a build volume with dimensions 500 mm × 240 mm × 220 mm. The GRIN lens itself measures 20 cm × 15 cm (as defined in the "Methods" section), matching the design domain (see Fig. 1b).

The printing process utilizes a phase-change wax as the support material, which is jetted in a molten state and solidifies upon cooling to provide stable support for overhanging features and internal cavities. Because the VCJ process is contactless, it can accommodate the wax support without smearing or mixing with the build material, enabling the fabrication of complex internal geometries such as the intricate gyroid lattice. Post-processing is straightforward: the completed build is heated to 65 °C to melt and drain the bulk of the support wax, heated in an inert fluid to post-cure the samples fully, followed by sonication in a heated cleaning solution to remove any residues. The result is a lightweight monolithic GRIN lens structure ready for integration into the measurement setup.

For rigorous experimental characterization, the manufactured lens was integrated into a bespoke PPW operating in the dominant quasi-TEM mode (qTEM), depicted in Fig. 1c. The PPW is formed by two metallic plates, placed at a distance less than half-wavelength at the maximum operating frequency to avoid excitation of higher-order modes. This GRIN-filled PPW creates a controlled environment that constrains the wave propagation to two dimensions, effectively simulating, by a multiple image process, an infinite medium in the perpendicular direction and producing the desired phase gradient on the opposite aperture. Along one edge, an array of standard waveguide ports serves as discrete input points. When a port is excited, it acts as a cylindrical wave source; the GRIN medium then intercepts and transforms this wave to provide a linear phase at the output boundary. This integrated prototype therefore realizes a Fourier-transform kernel directly at the material level, combining a simple feeding structure with a wave-shaping metamaterial core. In doing so, it eliminates the need for complex electronic beamforming networks composed of phase shifters, power dividers, and transmission lines. Moreover, imposing an arbitrary continuous one-dimensional function at the input boundary, realized through appropriate weighting of the discrete modal excitations at the ports, produces at the opposite boundary its spatial Fourier transform, provided that the significant spectral content of the input function lies within the accessible range of phase gradients supported by the device.

Physical mechanism

The core operational principle of the lens–how a simple change in feed location dictates a radical change in output angle–is elegantly visualized by examining the electromagnetic field within the PPW. Figure 2 presents snapshots of the steady-state electric field magnitude distributions. The three selected ports (Ports 3, 4, and 5) are representative of a continuous scanning range, while the three frequencies (13, 16, and 18 GHz) serve as discrete sample points across the operating bandwidth. Due to symmetry, only one half of the steering range is shown, with the opposite ports producing mirrored beam angles.

When the central port is activated (Port 3, left column), the emitted cylindrical wave encounters a symmetrically graded index medium. The lens periphery, with a lower refractive index, allows rays to travel faster, while the central, higher-index region slows them down. This symmetric velocity profile acts as a compensator, progressively bending the outwardly propagating wavefront until it emerges from the opposite side of the lens as parallel contours–a perfectly collimated plane wave propagating normal to the lens aperture (broadside, 0°). The field plots across all frequencies in the left column of Fig. 2 confirm this behavior, demonstrating consistent collimation across the entire 13–18 GHz band.

The mechanism for beam steering is revealed in the center and right columns of Fig. 2. Exciting Port 4 (center column), located to the right of the center, breaks the symmetry. The wave now enters a medium where the index gradient is no longer centered on its origin. The portion of the wavefront that propagates back toward the lens center travels through more of the higher-index, slower material than the portion spreading away from the center. This asymmetric phase delay systematically tilts the wavefront. The lens profile is specifically designed to convert this source displacement into a precise, constant phase slope across the output aperture. The result is a set of parallel wavefronts oriented at approximately 20°. Excitation of port 5 (right column), with the source on the extreme right, produces a steeper phase gradient due to greater displacement, thus steering the beam to a larger angle of 35°. Remarkably, this steering mechanism exhibits minimal frequency dependence: for each port, the wavefront orientation remains consistent throughout the 13–18 GHz band, as evidenced by the three rows in Fig. 2. This direct visualization confirms that beam steering is not achieved by time delays or phased interference outside the device but is fundamentally impressed upon the wave within the volumetric material itself, via a spatially engineered momentum exchange. The frequency stability can be understood analytically from the Eikonal formalism. The phase accumulation through the lens is $\phi(\omega) = k_0 \Psi$, where $\Psi = \int n(\mathbf{r})\, ds$ is the optical path length. The phase gradient at the aperture is therefore $d\phi/dx = k_0\, d\Psi/dx$. The steering angle then follows from the phase-gradient condition $\sin\theta = \frac{1}{k_0}\frac{d\phi}{dx} = \frac{d\Psi}{dx}$, which contains no frequency dependence. Thus, the beam pointing is intrinsically achromatic. Similarly, the device supports continuous spatial scanning: translating the feed to any intermediate position yields a corresponding intermediate linear phase gradient, producing a main beam that shifts continuously and monotonically between steering angles (Supplementary Fig. S5).

It is worth noting that in conventional GRIN-based Fourier optics lenses, such as the Mikaelian lens[36], the transformation is typically optimized

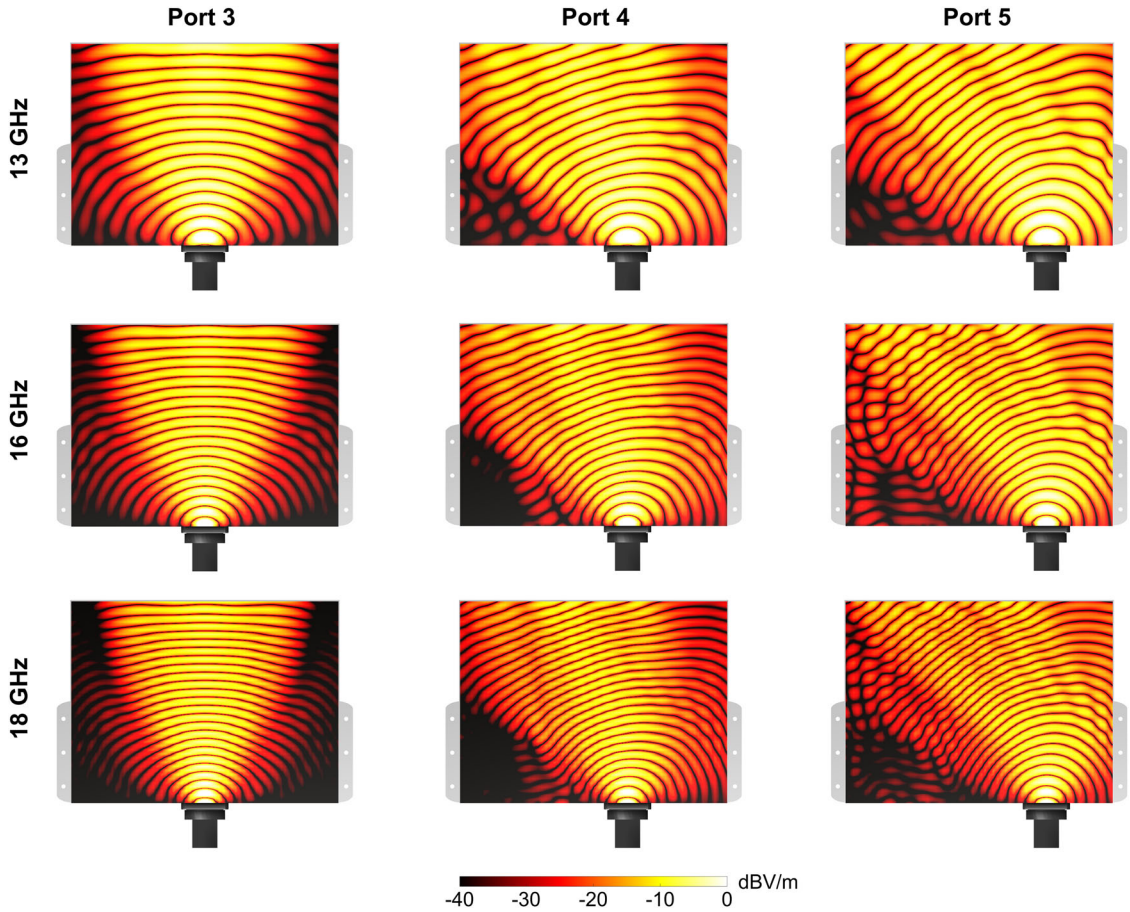


Fig. 2 | Near-field wavefront shaping inside the GRIN lens. The electric-field snapshot (in dBV/m) inside the parallel-plate waveguide is captured by simulation for three excitation frequencies (13, 16 and 18 GHz) and three different input ports (Ports 3--5). Rows correspond to increasing frequency, while columns correspond to different lateral positions of the excited port: central (Port 3, left column), intermediate (Port 4, center column), and extreme (Port 5, right column). Due to the symmetry of the structure, only one half of the steering range is shown; the opposite ports produce mirrored beam angles. The progressive tilting of the wavefronts with port displacement demonstrates broadband, port-controlled beam steering enabled by the GRIN medium.

for paraxial propagation and for mapping focused rays into a single parallel direction. In these systems, unfocused or off-axis source points produce beam tilts limited to a few beam waists and rapidly introduce aberrations[37]. By contrast, the proposed approach directly solves the governing wavefront transport equations, enabling a material-level realization of the Fourier kernel over a substantially larger angular domain, extending beyond the regimes explored in classical and analytical GRIN designs[30].

Far-field validation of broadband performance

The ultimate validation of any antenna lies in its radiation characteristics in the far-field. Figure 3 presents the antenna fabricated (a), the anechoic chamber measurement setup (b) and the comprehensive far-field radiation patterns across the operational bandwidth (c). Radiation data are presented as normalized patterns in the sine angular space (uv-space), where $u = \sin\theta\cos\phi$ and $v = \sin\theta\sin\phi$, providing a distortion-free view of beam directions. The right panels show the corresponding radiation patterns (gain in dBi) in the principal cut containing the device side walls.

Each column in Fig. 3c corresponds to a fixed input port, demonstrating the beam-steering function. The left column (Port 3) shows a dominant lobe firmly anchored at $u = 0$ (broadside, $\theta = 0^{\circ}$) across all three representative frequencies: 13, 16 and 18 GHz. The lobes are narrow, signifying high directivity, and exhibit well-suppressed sidelobes. The center column (Port 4) reveals the key result: the main beam is consistently displaced to $u \approx +0.34$ throughout the band. Using the relation $\theta = \arcsin(u)$, this corresponds to a physical steering angle of approximately 20°. Similarly, the right column (Port 5) shows the beam oriented to $u \approx +0.57$, corresponding to +35°. These values confirm the primary design goal: discrete port-selected beam steering in a ±35° range, as predicted by near-field observations. The remarkable consistency of the beam positions from 13 to 18 GHz underscores the truly broadband nature of the gradient-index mechanism, which is inherently less dispersive than resonant phase-shifting elements.

Examining the rows in Fig. 3c illustrates the bandwidth performance. At 13 GHz (top row), the beams are slightly wider–a consequence of the smaller electrical size of the lens at this lower frequency–but the steering is accurate and sidelobe control is maintained. At the center frequency of 16 GHz (middle row), the patterns are at their most optimal, with the tightest beamwidths and lowest sidelobes. At 18 GHz (bottom row), the lens operates at a larger electrical size, leading to even narrower beams and the emergence of finer structural details in the pattern, yet the beam pointing remains stable and no parasitic grating lobes appear. This stability is critical for wideband systems, such as satellite communications, where consistent coverage must be maintained across a wide swath of spectrum without recalibration. The clean, uncluttered patterns in all nine panels testify to the effectiveness of the continuous index gradient in providing smooth phase transformation, avoiding the diffraction artifacts and grating lobes typical of discrete-phase-array or stepped-index lenses. Finally, Fig. 3d provides a rigorous validation, where the right panels show the principal–cut radiation patterns (gain in dBi) for Ports 3, 4, and 5 at 13, 16, and 18 GHz, plotting measured co–polarized gain (solid lines) against full–wave simulated predictions (dashed lines).

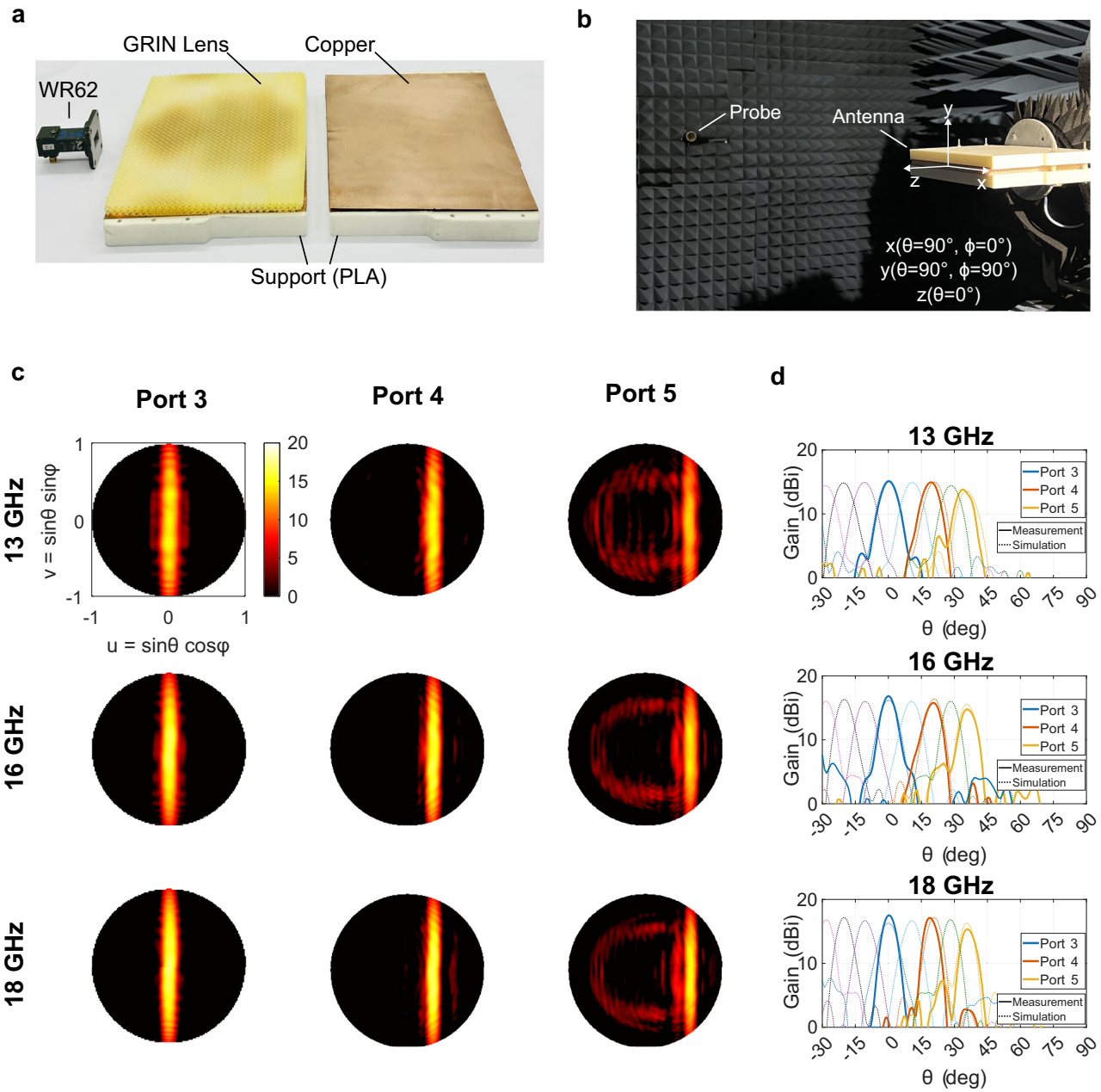


Fig. 3 | Fabricated prototype and far-field characterization. a Photograph of the monolithic GRIN lens fabricated via Vision-Controlled Jetting using Inkbit COT polymer. The intricate gyroid lattice is visible, with the graded density producing the desired permittivity distribution. **b** Anechoic chamber measurement setup showing the parallel-plate waveguide integrated with the GRIN lens and connected to a standard gain horn antenna. **c** Far-field radiation patterns in the u--v plane ($u = \sin\theta\cos\phi, v = \sin\theta\sin\phi$) for three operating frequencies (13, 16 and 18 GHz) and three input ports (Ports 3--5). Left column: Port 3 (central), center column: Port 4, right column: Port 5. Color maps show the normalized far-zone field magnitude, demonstrating frequency-robust beam steering controlled by the excited port. **d** Right panels show the corresponding radiation patterns (gain in dBi) in the principal cut for the Ports 3--5, highlighting well-defined, angularly separated fan beams across the operational bandwidth. Measurements are depicted in solid lines while full-wave simulations in dashed lines. Dashed lines superimposed on the experimental patterns trace the continuous evolution of the beam angle with feed displacement.

Measured performance and comparison with simulations

Figure 3d provides a rigorous validation, plotting the measured co-polarized gain (solid lines) against the full-wave simulated predictions (dashed lines) for Ports 3, 4, and 5 at 13, 16, and 18 GHz. The dashed lines superimposed on the experimental patterns in Fig. 3d trace the continuous evolution of the beam direction with feed displacement, which is further validated by additional simulations with nine ports across the band (Supplementary Figs. S5 and S6).

The agreement between measurement and simulation is striking across all cases. Not only do the main beam directions match precisely, but the intricate details of the sidelobe structures, the null positions, and the subtle beam broadening at lower frequencies are all faithfully reproduced. This close correlation serves a dual validation: it confirms the accuracy of our inverse-design and simulation tools, and it verifies the fabrication fidelity, proving that the printed gyroid metamaterial accurately implements the designed permittivity profile.

From these patterns, key performance metrics are extracted. The lens achieves a measured peak gain of 16.8 dBi at 16 GHz for the broadside beam (Port 3). More importantly, the gain remains high for the steered beams. The variation in peak gain when switching from the broadside port to the extreme steering ports–a metric known as scan loss–is less than 2 dB across the entire band. This low scan loss indicates

high aperture efficiency regardless of beam direction, a result of the lens's excellent impedance matching and minimal spillover loss, inherent advantages of the graded-index taper. The 3-dB gain bandwidth, observed by tracking the peak gain at each port, extends over the 13–18 GHz range (a 33% fractional bandwidth), far exceeding the typical 10–15% bandwidth of many fixed-beam and phased-array solutions based on resonant elements.

To assess the role of continuous grading, we thresholded our optimized profile into a binary distribution (ε_r=1.1 and 2.0), keeping all other parameters identical (Supplementary Fig. S1). Full–wave simulations (Supplementary Fig. S2) show that although the binary structure still generates steering (even overscanning to 40° at the extreme port), the abrupt interfaces introduce Fresnel reflections and scattering, reducing the realized gain by 3–5 dB across the entire band. This confirms that the continuous profile is essential for maintaining the reported low scan loss and high aperture efficiency, while the phase accumulation itself remains achromatic due to the propagation–based nature of the device.

The observed degradation at the extreme steering angle (35°) is intrinsic to the chosen permittivity range (ε_r = 1.1 to 2.0), as confirmed by the excellent agreement between simulation and measurement (Fig. 3d), ruling out experimental error. To demonstrate scalability, we performed an additional simulation with an extended range (ε_r = 1.0 to 5.0), which enables beam steering up to ±50° with significantly reduced aberrations (Supplementary Figs. S3 and S4). The choice of permittivity range thus represents a trade-off between manufacturability and scan range, and higher-contrast designs can achieve wider steering with improved pattern fidelity.

To further confirm the continuous frequency response, Supplementary Fig. S6 presents additional far-field patterns at 14 GHz and 17 GHz–intermediate frequencies between the three design points. The main beam positions remain stable at the expected angles, and the gain varies smoothly, consistent with the achromatic phase response derived in the Physical mechanism section.

The system-level implication is profound. This single passive dielectric component, illuminated by a simple switch that selects one of several fixed feeds, replicates the core functionality of an active beamforming network. It provides discrete, high-gain beam positions with low loss and ultra-wide bandwidth. When compared to traditional solutions–the bulky, lossy corporate feeds of a Rotman lens or the complex, narrowband cascaded couplers of a Butler matrix–this GRIN lens prototype demonstrates a paradigm of exceptional simplicity and performance. It eliminates all internal conductors, resistors, and complex transmission line layouts, replacing them with a shaped dielectric, thereby offering a pathway to lower-cost, lighter-weight, and more efficient beam-steering frontends for future satellite terminals, automotive radar modules, and fixed wireless access points. The data clearly demonstrate that inverse-designed metamaterial GRIN lenses are a viable and superior technology for modern multi-beam systems.

Discussion

The inverse-designed GRIN platform presented in this work implements the kernel of a one-dimensional Fourier transform with a fidelity that significantly exceeds that achievable using conventional Fourier-optics lenses. Classical GRIN and Fourier lenses, such as the Mikaelian lens, are typically optimized for paraxial propagation and for mapping focused rays into a single parallel direction[36]. In these systems, unfocused or off-axis source points produce beam tilts limited to a few beam waists and rapidly introduce aberrations, resulting in a poor approximation of the ideal Fourier kernel. By contrast, the proposed approach directly solves the governing wavefront transport equations, enabling a material-level realization of the Fourier kernel over a substantially larger angular domain.

From an antenna-engineering perspective, it is important to note that one-port–one-beam operation can be achieved using a variety of established techniques. However, the GRIN-based implementation demonstrated here combines this functionality with a large operational bandwidth while maintaining flat input and output boundaries, which are highly desirable for practical antenna integration. The flat geometry simplifies feeding and packaging, while the broadband response arises from continuous material modulation rather than from frequency-sensitive phase-shifting networks. Moreover, the concept naturally extends beyond a one-dimensional aperture: overlapping PPWs or exploiting rotational symmetry can directly enable two-dimensional antenna apertures without a corresponding increase in system complexity.

When compared with established beamforming architectures such as Rotman lenses[33], the proposed GRIN Fourier-transform device offers a fundamentally different trade-off. Rotman lenses rely on geometrical path-length equalization and are intrinsically constrained by phase errors that grow with scan angle and bandwidth. In contrast, the present method leverages continuous refractive-index modulation to produce smoother phase gradients and reduced aberrations over extended scan ranges. Relative to Butler matrices[34], which implement discrete Fourier transforms through cascaded hybrids and phase shifters, the proposed approach replaces complex, lossy and frequency-sensitive electronic networks with a passive, monolithic structure that performs the transformation directly within the electromagnetic medium, naturally scaling to higher port counts without exponential growth in circuit complexity.

To clarify the merits of our approach, Table 1 compares the key features of our GRIN lens with Rotman lenses and Butler matrices. The continuous scanning, wide bandwidth, and structural simplicity of our device stem from the direct material–level encoding of the Fourier kernel, which replaces complex feed networks with a single passive dielectric.

More broadly, this work aligns with the emerging paradigm of analog and physical computing, in which mathematical operations are executed directly through wave–matter interactions rather than through digital electronics[38,39]. By encoding the Fourier-transform kernel within the spatial permittivity distribution of a passive medium, the proposed device exemplifies material-embedded computation and highlights a pathway toward scalable, low-loss, and broadband wave-based processors operating across microwave and optical frequencies. While the lens itself is achromatic, the practical system bandwidth is bounded by three factors. First, the lower–frequency limit is set by the electrical size: the lens must remain electrically large for GO to be valid; scaling the physical dimensions proportionally extends operation to lower frequencies. Second, the upper–frequency limit is set by the effective–medium approximation: the gyroid unit cell must remain deeply sub–wavelength; improved fabrication resolution would push this limit. Third, the WR62 feed transition constrains the overall system bandwidth; a broader–band feed would extend the total operational range.

Table 1 | Comparison of passive beamforming architectures

Aspect	Rotman Lens[33]	Butler Matrix[34]	This Work
Steering	Discrete	Discrete	**Continuous**
Beam positions	Fixed ports	Fixed beams	**Arbitrary**
Bandwidth	Limited	Narrowband	**33% (13–18 GHz)**
Scan range	± 30° – – ± 45°	Fixed	± **35°** (extendable)
Scan loss	2–4 dB	Network-dependent	**<2 dB**
Design time	Iterative	Circuit synthesis	**Minutes (PC)**
Internal elements	Conductors/dielectrics	Hybrids/phase shifters	**None (monolithic)**
Loss mechanism	Dielectric/conductor	Hybrid/phase shifter	**Low-loss dielectric**
Scalability	Moderate	Exponential growth	**Flexible**

Key advantages are in **bold**.

Methods

Geometrical optics model and LFSM solver

The analysis of graded-index (GRIN) lenses is performed within the framework of geometrical optics (GO), under the assumption of a slowly varying refractive index relative to the wavelength. The electric field is expressed in asymptotic form as

$$\mathbf{E}(\mathbf{r}) = \hat{\mathbf{e}}(\mathbf{r})A(\mathbf{r})e^{-jk\Phi(\mathbf{r})}, \tag{1}$$

where $\Phi(\mathbf{r})$ is the normalized phase (eikonal), $A(\mathbf{r})$ is the amplitude, $\hat{\mathbf{e}}(\mathbf{r})$ is the polarization vector, and k is the free-space wavenumber. The phase and amplitude satisfy the Eikonal equation and the Energy Transport equation, respectively.

To solve these equations efficiently and accurately, we employ the Lax-Friedrichs sweeping method (LFSM)[32], a fast iterative solver that operates on a Cartesian grid. Unlike traditional ray tracing methods[5], the LFSM avoids caustic problems and spatial discontinuities by solving the governing partial differential equations directly on the computational grid. The method is applied to factorized forms of the Eikonal and transport equations, which remove the singularities introduced by point or line sources, enabling high-accuracy computation of both phase and amplitude distributions within the lens volume. A complete description of the LFSM algorithm and its validation can be found in our earlier work[32].

Inverse design optimization framework

The inverse design problem is formulated as a constrained optimization over the spatial distribution of the relative permittivity $\epsilon(\mathbf{r}) = n^2(\mathbf{r})$. The design domain is a rectangular region in the xz-plane with width $a = 20$ cm and length $b = 15$ cm. To reduce the number of design variables while leveraging the symmetry of the structure, a set of 9 control points is defined only on the right half of the domain ($x > 0$), with the permittivity distribution mirrored across the z-axis. This configuration provides a balanced trade-off between design flexibility and intrinsic regularization, effectively preventing overfitting and non-physical oscillations. The x-coordinate of the control points ranges from $x = 0$ to $x = 10$ cm, and the z-coordinate ranges from $z = 0$ to $z = 15$ cm. The permittivity at control points located on the domain edges is fixed at $\epsilon = 1.1$ to ensure a smooth transition and minimize reflections at the lens boundaries. The permittivity values at the remaining grid points are assigned via bilinear interpolation from the control points, ensuring a smooth gradient. The optimization is subject to a manufacturability constraint on the permittivity

$$1.1 \le \epsilon(\mathbf{r}) \le 2.0. \tag{2}$$

For the multi-beam lens, we define 3 discrete source positions (input ports) and their corresponding target phase distributions at the output aperture. The first source, located at $(x_s, z_s) = (0, 0)$, is designed to generate a broadside beam. The second source, located at (2.5cm, 0), is designed to steer the beam to $\theta = 20^\circ$. The third source, located at (5.0cm, 0), is designed to steer the beam to $\theta = 35^\circ$. The target phase for the i-th beam is a linear function:

$$\bar{\psi}_i(\bar{x}) = \bar{x}\sin\theta_i, \tag{3}$$

where $\bar{x}$ is the coordinate along the output aperture and θ_i is the desired steering angle. The objective function to be minimized is the weighted sum of phase errors across all beams, normalized by the amplitude distribution to emphasize regions of high energy:

$$\mathcal{F} = \sum_{i=1}^{N} \frac{\int_{\bar{x}} \left[\Phi_i(\bar{x}) - \bar{\psi}_i(\bar{x})\right]^2 A_i(\bar{x})\, d\bar{x}}{\int_{\bar{x}} A_i(\bar{x})\, d\bar{x}}, \tag{4}$$

where Φ_i and A_i are the phase and amplitude at the output aperture for excitation at the i-th port, computed by the LFSM solver for a given permittivity distribution.

The amplitude weighting $A_i(\bar{x})$ in Eq. (4) explicitly ensures that phase errors in regions of low field intensity contribute negligibly to the objective function. This prevents the optimizer from converging to an unphysical solution, such as a tightly focused Gaussian spot that would satisfy the phase-only criterion but diverge rapidly in the far field. More fundamentally, the underlying physics already guarantees that the far-field performance is not compromised by amplitude-induced aberrations. For the aperture field $E(\bar{x}) = A(\bar{x})e^{jk_0\Phi(\bar{x})}$, the far-field pattern is $E_{ff}(\theta) \propto \int A(\bar{x})e^{jk_0(\Phi(\bar{x})-\bar{x}\sin\theta)}d\bar{x}$. The stationary-phase condition yields $d\Phi/d\bar{x} = \sin\theta$. Hence, enforcing the target linear phase $\Phi(\bar{x}) = \bar{x}\sin\theta_i$ via Eq.(3) directly fixes the main beam at $\theta = \theta_i$, regardless of the specific amplitude distribution $A(\bar{x})$. The weighting in Eq. (4) thus serves as an additional numerical safeguard, but the beam pointing itself is fundamentally dictated by the phase gradient alone, as confirmed by the excellent agreement between simulation and measurement in Fig. 3d.

The gradient of the objective function with respect to the control point permittivities is computed using a finite-difference approach. The optimization loop is implemented in MATLAB using the `fmincon` solver with the interior-point algorithm, which handles the bound constraints efficiently. Each optimization run typically requires over 1000 iterations, with each iteration performing multiple LFSM evaluations. The total computation time is a few minutes on a standard desktop computer. Notably, the scanning range can be extended by increasing the maximum permittivity, as the larger index contrast allows for greater phase accumulation across the aperture. The use of only nine control points is deliberate, exploiting the physical smoothness of GRIN profiles for propagation–based beamforming. Unlike scattering structures requiring voxel-level resolution, this low–dimensional parametrization avoids the computational overhead of adjoint–based topology optimization while remaining fully adequate for the present class of devices.

Data availability

The datasets generated during and/or analysed during the current study are available from the corresponding author on reasonable request. Data are stored at the University of Siena and can be accessed by contacting Ilir Gashi (ilir.gashi2@unisi.it).

Code availability

The custom code used for the Lax-Friedrichs sweeping method (LFSM) solver and the inverse-design optimization framework is available from the corresponding author upon reasonable request. The MATLAB optimization routine uses the built-in `fmincon` solver (interior-point algorithm). A compiled version of the code is available for reproducibility purposes, upon reasonable request.

Received: 21 May 2026; Accepted: 4 September 2026;
Published online: 26 September 2026

References

1. Pendry, J. B., Schurig, D. & Smith, D. R. Controlling electromagnetic fields. *Science* **312**, 1780–1782, https://doi.org/10.1126/science.1125907 (2006).
2. Smith, D. R. et al. Metamaterials and negative refractive index. *Science* **305**, 788–792, https://doi.org/10.1126/science.1096796 (2004).
3. Yu, N. et al. Light propagation with phase discontinuities: generalized laws of reflection and refraction. *Science* **334**, 333–337, https://doi.org/10.1126/science.1210713 (2011).
4. Valentine, J. et al. Three-dimensional optical metamaterial with a negative refractive index. *Nature* **455**, 376–379, https://doi.org/10.1038/nature07247 (2008).

5. Gashi, I., Paraskevopoulos, A., Maci, S. & Albani, M. Go analysis of grin lens antennas by combining in a single ode, field and wavefront-curvature transport to the ray tracing. *IEEE Trans. Antennas Propag.* **72**, 2147–2160, https://doi.org/10.1109/TAP.2024.3360727 (2024).
6. Glybovski, S. B. et al. Metasurfaces: From microwaves to visible. *Phys. Rep.* **634**, 1–72, https://doi.org/10.1016/j.physrep.2016.04.004 (2016).
7. Genevet, P. et al. Recent advances in planar optics: from gradient-index lenses to surface waves. *Optica* **4**, 139–152, https://doi.org/10.1364/OPTICA.4.000139 (2017).
8. Kildishev, A. V. et al. Planar photonics with metasurfaces. *Science* **339**, 1232009, https://doi.org/10.1126/science.1232009 (2013).
9. Zheludev, N. I. et al. Roadmap on electromagnetic metamaterials and metasurfaces. *J. Phys. Photonics* **6**, 032502, https://doi.org/10.1088/2515-7647/ad1a3b (2024).
10. Ma, Q. et al. Inverse design of material, structure, and process for dielectric properties of additively manufactured pla/batio3 polymer composites. *Compos. Commun.* https://doi.org/10.1016/j.coco.2025.102314 (2025).
11. Buchner, T. J. K. et al. Vision-controlled jetting for composite systems and robots. *Nature* **623**, 522–530, https://doi.org/10.1038/s41586-023-06684-3 (2023).
12. Bonner, C. et al. Fabrication and analysis of electrically large Luneburg lenses using vision-controlled material jetting. *Opt. Eng.* **65**, 025104, https://doi.org/10.1117/1.OE.65.2.025104 (2026).
13. Esfandiari, M. et al. Additively manufactured metasurfaces and metamaterials: designs, fabrications, and applications from microwave to photonics. *APL Photonics* **10**, 041101, https://doi.org/10.1063/5.0241299 (2025).
14. Kadic, M. et al. 3d metamaterials. *Nat. Rev. Phys.* **1**, 198–210, https://doi.org/10.1038/s42254-018-0018-y (2019).
15. Zhu, J. et al. High-efficiency and wideband multifunctional lenses based on 3d printed gradient index structures. *Adv. Sci.* **10**, 2300586, https://doi.org/10.1002/advs.202300586 (2023).
16. Roberts, G. et al. 3D-patterned inverse-designed mid-infrared metaoptics. *Nat. Commun.* **14**, 2768. https://doi.org/10.1038/s41467-023-38258-2 (2023).
17. Roques-Carmes, C. et al. Toward 3D-printed inverse-designed metaoptics. *ACS Photonics* **9**, 43–51, https://doi.org/10.1021/acsphotonics.1c01442 (2022).
18. Molesky, S. et al. Inverse design in nanophotonics. *Nat. Photonics* **12**, 659–670, https://doi.org/10.1038/s41566-018-0246-9 (2018).
19. Li, Z. et al. Empowering metasurfaces with inverse design: principles and applications. *ACS Photonics* **9**, 2178–2192, https://doi.org/10.1021/acsphotonics.1c01850 (2022).
20. Li, Z. et al. Inverse design enables large-scale high-performance meta-optics reshaping virtual reality. *Nat. Commun.* **13**, 2409. https://doi.org/10.1038/s41467-022-29973-3 (2022).
21. Jensen, J. S. & Sigmund, O. Topology optimization for nanophotonics. *Laser Photonics Rev.* **5**, 308–321, https://doi.org/10.1002/lpor.201000014 (2011).
22. Lalau-Keraly, C. M. et al. Adjoint shape optimization applied to electromagnetic design. *Opt. Express* **21**, 21693–21701, https://doi.org/10.1364/OE.21.021693 (2013).
23. Ji, W. et al. Recent advances in metasurface design and quantum optics applications with machine learning, physics-informed neural networks, and topology optimization methods. *Light Sci. Appl.* **12**, 169, https://doi.org/10.1038/s41377-023-01218-y (2023).
24. Overvig, A. C. et al. Dielectric metasurfaces for complete and independent control of the optical phase and amplitude. *Light Sci. Appl.* **8**, 32, https://doi.org/10.1038/s41377-019-0201-7 (2019).
25. Barré, N. & Jesacher, A. Inverse design of gradient-index volume multimode converters. *Opt. Express* **30**, 10573–10586, https://doi.org/10.1364/OE.451704 (2022).
26. Nanda, A. et al. 3d integrated optics enabled by inverse design and multi-photon lithography. *Opt. Lett.* https://doi.org/10.1364/OL.590077 (2026).
27. So, S. et al. Multicolor and 3d holography generated by inverse-designed single cell metasurfaces. *Adv. Mater.* **35**, 2208520, https://doi.org/10.1002/adma.202208520 (2023).
28. Ma, H. et al. Inverse-design-assisted on-chip grin meta-lens for dual-polarization multimode waveguide crossing. *ACS Photonics* **12**, 1953–1961, https://doi.org/10.1021/acsphotonics.4c02391 (2025).
29. Williams, J. J. et al. Shrinking a gradient-index-lens antenna system with a spaceplate. *Phys. Rev. Appl.* **22**, 034039, https://doi.org/10.1103/PhysRevApplied.22.034039 (2024).
30. Paraskevopoulos, A., Gashi, I., Albani, M. & Maci, S. Analytical formulas for refractive indices of a telescopic grin lens for aperture magnification. *IEEE Antennas Wirel. Propag. Lett.* **21**, 2206–2210, https://doi.org/10.1109/LAWP.2022.3203914 (2022).
31. Gashi, I., Maci, S. & Albani, M. Analytical inverse design of grin lens antennas: The phase tracing method. *IEEE Trans. Antennas Propag.* 1–1, https://doi.org/10.1109/TAP.2026.3676548 (2026).
32. Gashi, I., Maci, S. & Albani, M. Numerical solution of the eikonal and transport equations for grin lens antennas by using the Lax–Friedrichs sweeping method. *IEEE Trans. Antennas Propag.* **73**, 6686–6696, https://doi.org/10.1109/TAP.2025.3572618 (2025).
33. Rotman, W. & Turner, R. Wide-angle microwave lens for line source applications. *IEEE Trans. Antennas Propag.* **11**, 623–632, https://doi.org/10.1109/TAP.1963.1138114 (1963).
34. Butler, J. & Lowe, R. Beam-forming matrix simplifies design of electronically scanned antennas. *Electron. Des.* **9**, 170–173 (1961).
35. Ataloglou, V. G. et al. Metasurfaces: physics and applications in wireless communications. *Natl. Sci. Rev.* **10**, 164, https://doi.org/10.1093/nsr/nwad164 (2023).
36. Mikaelian, A. L. & Prokhorov, A. M. Self-focusing media with variable index of refraction. in *Progress in Optics*, Vol. 17 (eds Wolf, E.) 283–346 (North-Holland, Amsterdam, 1980).
37. Paraskevopoulos, A., Maggiorelli, F., Albani, M. & Maci, S. Radial GRIN lenses based on the solution of a regularized ray congruence equation. *IEEE Trans. Antennas Propag.* **70**, 1284–1294, https://doi.org/10.1109/TAP.2021.3111315 (2022).
38. Engheta, N. Circuits with light at nanoscales: optical nanocircuits inspired by metamaterials. *Science* **317**, 1698–1702, https://doi.org/10.1126/science.1133268 (2007).
39. Silva, A. et al. Performing mathematical operations with metamaterials. *Science* **343**, 160–163, https://doi.org/10.1126/science.1242818 (2014).

Acknowledgements

This work was funded by Huawei inside the framework of the Huawei–University of Siena Joint Laboratory.

Author contributions

I.G., S.M., and M.A. conceived the inverse-design framework and formulated the optimization problem. I.G. implemented the Lax-Friedrichs sweeping method solver and performed the numerical simulations. S.T. and Z.N. developed the Vision-Controlled Jetting fabrication process and manufactured the GRIN lens prototype. I.G. and M.A. designed the experimental setup and analyzed the measurement data. I.G. wrote the initial manuscript draft. All authors discussed the results, contributed to the interpretation of the data, and reviewed and edited the manuscript.

Funding

This work was funded by Huawei inside the framework of Huawei – University of Siena Joint Laboratory.

Competing interests

The authors declare no competing interests.

Additional information

Supplementary information The online version contains supplementary material available at https://doi.org/10.1038/s44172-026-00787-1.

Correspondence and requests for materials should be addressed to Ilir Gashi.

Peer review information *Communications Engineering* thanks Weiming Zhu and the other, anonymous, reviewer(s) for their contribution to the peer review of this work. Primary Handling Editors: [Wenjie Wang]. A peer review file is available.

Reprints and permissions information is available at http://www.nature.com/reprints

Publisher's note Springer Nature remains neutral with regard to jurisdictional claims in published maps and institutional affiliations.

Open Access This article is licensed under a Creative Commons Attribution 4.0 International License, which permits use, sharing, adaptation, distribution and reproduction in any medium or format, as long as you give appropriate credit to the original author(s) and the source, provide a link to the Creative Commons licence, and indicate if changes were made. The images or other third party material in this article are included in the article's Creative Commons licence, unless indicated otherwise in a credit line to the material. If material is not included in the article's Creative Commons licence and your intended use is not permitted by statutory regulation or exceeds the permitted use, you will need to obtain permission directly from the copyright holder. To view a copy of this licence, visit http://creativecommons.org/licenses/by/4.0/.

© The Author(s) 2026

This Article in Press is shared early to give you faster access to new research. It is citable and carries a permanent DOI. The final edited version will replace it automatically.